


# Investigation of in-cylinder soot formation in a DISI engine during transient operation by simultaneous endoscopic PIV and flame imaging

International J of Engine Research  
2023, Vol. 24(3) 1175–1189  
© IMechE 2022  
Article reuse guidelines:  
sagepub.com/journals-permissions  
DOI: 10.1177/14680874221079764  
journals.sagepub.com/home/jer  


Christian Fach<sup>1</sup> , Nico Rödel<sup>2</sup>, Jürgen Schorr<sup>3</sup>, Christian Krüger<sup>3</sup>,  
Andreas Dreizler<sup>1</sup> and Benjamin Böhm<sup>1</sup>

## Abstract

A single-cylinder full-metal engine with a real combustion chamber geometry was used to investigate particulate number emissions resulting from transient engine operation. The formation of particulate number emissions depends on mixture formation influenced by the in-cylinder flow and injection, and the formation of fuel films on the in-cylinder walls. For the investigation of this multi-parameter process, simultaneous endoscopic PIV and combustion visualization were applied. Hence, the measurement techniques allowed the investigation of in-cylinder flow, flame propagation, and soot formation. The test rig was modified to apply a generic load step and a realistic tip-in with Miller cycle. The reproducibility of the engine parameters during the transient allowed statistical analysis and the comparison between steady-state operating points. Cause-and-effect chains concerning the formation of soot are concluded by correlation analysis of parameters extracted from the flow field, the flame propagation and the soot luminosity.

## Keywords

High-speed particle image velocimetry, spray visualization, flame propagation, soot formation, endoscopic, internal combustion engine, transient engine operation

Date received: 1 November 2021; accepted: 24 January 2022

## Introduction

One challenge for the development of direct-injection spark ignition (DISI) engines is the limitation of particulate number emissions, which was introduced with the EURO 6 standard<sup>1</sup> and is expected to be further tightened with the EURO 7 standard. Another challenge is the introduction of new test procedures that also take into account highly dynamic transient operation, such as the Worldwide Harmonized Light-duty vehicles Test Procedure (WLTP) and real driving emissions.<sup>2</sup> Hence, transient engine operation, which can lead to increased particulate number (PN) emissions, must be taken into account during the development phase.

Load steps or tip-ins are maneuvers which can cause an increase in pollutant emissions.<sup>3–5</sup> During these maneuvers, PN emission of the transient operation can be significantly higher than emissions from the corresponding stationary operation. This presents a particular challenge for engine parameterization, such as control of gas exchange, ignition and injection timing.

Investigations by Sabathil et al.<sup>6</sup> showed that load-steps can also result in higher PN emissions than the corresponding stationary operation. Hadler et al.<sup>7</sup> investigated the effect of injection strategies on PN emissions in the exhaust of a DISI engine. They concluded that the investigated split injection strategy was more sensitive to variations in engine parameters.

<sup>1</sup>Fachgebiet Reaktive Strömungen und Messtechnik, Technische Universität Darmstadt, Darmstadt, Germany

<sup>2</sup>Mercedes-Benz AG, Kirchheim unter Teck, Germany

<sup>3</sup>Mercedes-Benz AG, Stuttgart, Germany

### Corresponding authors:

Christian Fach, Fachgebiet Reaktive Strömungen und Messtechnik, Technische Universität Darmstadt, Otto-Berndt-Str. 3, Darmstadt 64287, Germany.  
Email: fach@rsm.tu-darmstadt.de

Benjamin Böhm, Fachgebiet Reaktive Strömungen und Messtechnik, Technische Universität Darmstadt, Otto-Berndt-Str. 3, Darmstadt 64287, Germany.  
Email: boehm@rsm.tu-darmstadt.de

**Table 1.** Specifications of the endoscopic engine.

Displacement volume	373 cm <sup>3</sup>
Cylinder offset	12 mm
Coolant temperature	85°C
Oil temperature	55°C
Fuel	Gasoline E10
Injection pressure	350 bar

The injection timing influences the fuel-wall interaction. Hereby, the fuel interacts with the liner wall, piston surface, valves or injector tip. These interactions can lead to the formation of fuel films of the surfaces which result in sooty combustion,<sup>8–10</sup> for example, pool fires at piston surfaces. The cylinder wall temperature and the gas phase temperature further influence the formation of fuel films and soot.<sup>11</sup>

For investigating cause-and-effect chains, time-resolved optical measurement techniques have proven useful in providing the necessary information of the in-cylinder processes. These are often applied to optically accessible engines, which are used to investigate specific engine phenomena in detail<sup>12–14</sup> or to collect data for the validation of simulations.<sup>15–17</sup> Optical engines are well suited for the investigation of the flow field as well as the early phase of combustion. However, the large-area optical accesses exhibit altered heat transfer compared to real engines, resulting in higher surface temperatures<sup>18</sup> as well as differences in the in-cylinder pressure traces during combustion and the formation of pollutant emissions.<sup>19</sup> Since the formation of fuel films and hence soot depends on surface temperature and heat transfer, full-metal engines with minimally-invasive optical accesses are better suited for investigating soot formation.

Endoscopic imaging has been successfully applied to full-metal engines for the investigation of in-cylinder processes.<sup>20–23</sup> In a previous study, a multi-parameter imaging approach was introduced for the investigation of the in-cylinder flow, flame propagation and soot formation during transient engine operation.<sup>24</sup> Simultaneous endoscopic particle image velocimetry (PIV) and imaging of flame propagation and soot luminosity were applied to a single-cylinder DISI engine with combustion chamber geometry as in pre-production-type engines. The endoscopic PIV was verified by a comparison measurement at both the endoscopic engine and the equivalent optical engine. The analysis of the in-cylinder flow field during the late compression stroke, flame propagation and soot luminosity of single cycles during a tip-in maneuver indicated cause-and-effect chains for the formation of pool fire and soot at the injector tip.

The aim of this work was to investigate the interactions between the in-cylinder processes during the transients. Therefore, statistical analysis of the simultaneous multi-parameter measurements was performed during transient and steady-state operation

points. Comparing transient and steady-state operation points, the effect of the transient operation on the in-cylinder processes was analyzed. To the best of the author's knowledge, this work presents the first correlation analysis used to investigate cause-and-effect chains during transient engine operation.

## Experimental set up

### Endoscopic-engine

The measurements were performed in a single-cylinder DISI engine introduced in Fach et al.<sup>24</sup> The engine was equipped with a four-valve cylinder head. The spark plug was placed between the exhaust valves and the multi-hole injector (Bosch HDEV 6) was located in the central symmetry plane. The pre-production combustion chamber had a bore and stroke of 78 mm. To lubricate the liner, engine oil was delivered through the piston, which was equipped with production-type piston rings and had a top-land height of 7 mm. The resulting compression ratio was about 10.1. Table 1 contains further engine specifications.

Optical access to the combustion chamber was enabled by an endoscope with a front diameter of 12 mm, which was located in the cylinder head between the intake valves IV and exhaust valves EV, as shown in Figure 1. In addition, the cylinder liner was equipped with two sapphire glass windows which were located along the central symmetry plane and flush-mounted with the cylinder wall. Hence, the windows had curved inner surfaces and acted as negative focal length lenses. This prevented blow-by and ensured that the oil was sufficiently well wiped off the windows by the piston rings. The window between the intake valves, with a width of 8 mm and a height of 70 mm respectively, was used as laser access. The window enabled an almost non-divergent laser sheet, applying the top-land of the corresponding production engine. The other window with a diameter of 8 mm was used for laser alignment on the opposite side of the cylinder between the exhaust valves.

For realistic transient engine operation, modifications were made with regard to gas exchange, intake manifold pressure control, injection and ignition. A hydraulic active valve train system (Lotus AVT) enabled cyclic variations of valve timing and valve lift. The time of ignition TOI and start of injection SOI were controlled using a flexible engine control unit (IAV Flexible Injection and Ignition for Rapid Engineering, FI<sup>2RE</sup>). The pressure inside the pressure vessel was set to 1.2 bar and controlled by a mass flow controller. A throttle was used for intake manifold pressure control, allowing realistic intake manifold pressure gradients. Downstream from the throttle, silicone oil droplets were seeded (Palas AGF 10.0D) through two opposing jet-in-crossflow arrangements to ensure homogenous mixing with the intake air for the PIV measurements. The mass flow through the seeder was controlled by an

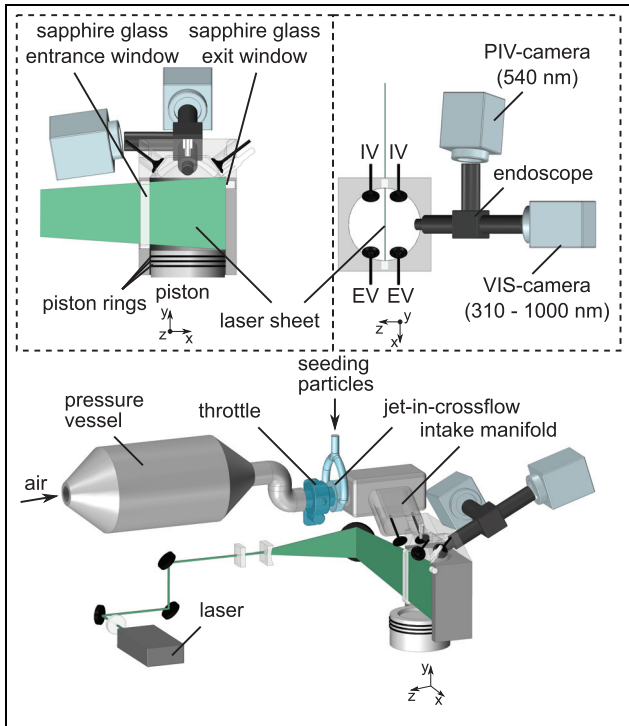


**Figure 1.** Experimental setup for simultaneous endoscopic PIV and flame and soot imaging during transient operation.

electric proportional needle valve, which allowed compensation for varying seeding density during transient operation. Within a parametric table, the engine parameters and the synchronization triggers of the measurement technique were set time-based for each individual cycle.

**Operational conditions**

*Load step.* A generic load step was performed at 1400 rpm with an SOI of  $-270\text{CA}^\circ\text{aTDC}$ . To minimize the influence of internal gas recirculation and exhaust manifold pressure fluctuations, intake valve opening and exhaust valve closing were set to  $20^\circ\text{CA}$  after gas exchange TDC and  $-20^\circ\text{CA}$  after gas exchange TDC. Conventional valve lifts and cam profiles were applied. The load step was characterized by the highest possible intake manifold pressure gradient or load gradient. Figure 2 shows the evolution of the phase-averaged intake manifold pressure, IMEP, and 50% mass fraction burned MFB50 along the load step. The phase-averaged intake manifold pressure increased from about 0.43 bar to 0.68 bar within cycles 4–7, resulting in a load increase, indicated by the IMEP, from 2.7 to 5.4 bar. Beginning with cycle 8, the engine parameter settings remained unchanged until cycle 14 of the load step. The TOI was controlled to keep MFB50 at  $7^\circ\text{CAaTDC}$ . After each load step, additional 189 cycles were parameterized, allowing for good reproducibility as indicated by the standard deviations of the engine parameters (gray areas in Figure 2). All 203 cycles refer

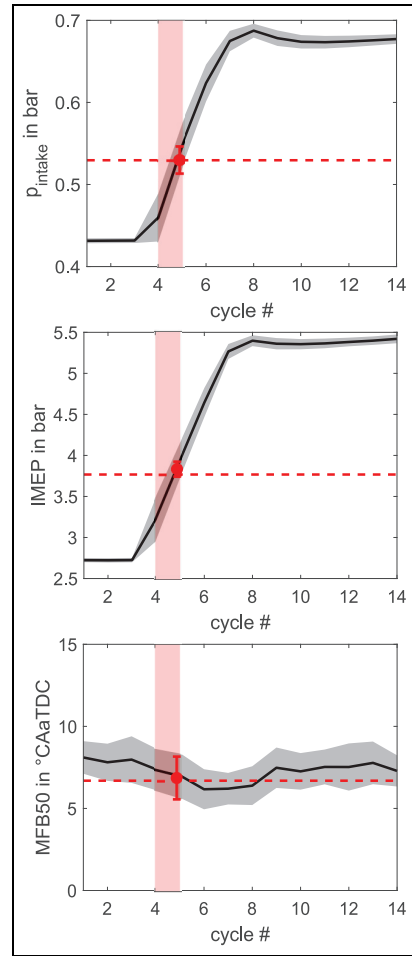


**Figure 2.** Intake manifold pressure (top), indicated mean effective pressure IMEP (middle) and 50% mass fraction burned MFB50 (bottom) along the cycles of the load step. Black lines indicate the phase-average and the gray area one standard deviation. The average of transient operating point TOP (rectangle) is indicated by the dot and the average of stationary operating point SOP by the dashed line.

to a single repetition of the load step. A total of 68 repetitions were performed. The evolution of intake manifold pressure and IMEP during three consecutive repetitions is shown in Figure 3.

For the investigation of transient engine operation, the transient operating point TOP was compared with the corresponding stationary operating point SOP, whose engine parameters are summarized in Table 2.

*Tip-in.* Several studies have shown that a tip-in leads to a significant increase in PN emissions.<sup>3,7,20</sup> This was also observed for a tip-in during a WLTC of the corresponding four-cylinder engine with the same combustion chamber geometry as in this study. Since the maneuver did not exhibit significant cycle-to-cycle variations at an engine speed of about 1400 rpm and start of injection at  $-290^\circ\text{CAaTDC}$ , it was well suited for the investigation of the in-cylinder flow, flame propagation, soot formation also in comparison to the load step

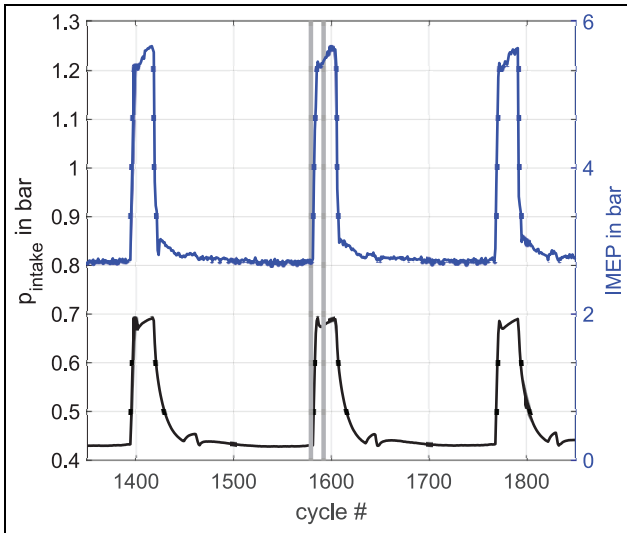


**Figure 3.** Intake manifold pressure (black line) and indicated mean effective pressure IMEP (blue line) along three consecutive repetitions. Gray lines indicate cycle 1 and 14 of a single load step.

described before. The tip-in included 10 cycles of motored engine operation. During the following 37 cycles a load step was performed with Miller cycle which was realized by asymmetric and reduced valve lifts. The first cycle of the load step is denoted as cycle 1 in the following. The evolution of the phase-averaged engine parameters (black lines) is given in Figure 4. Figure 4(a) shows the evolution of the intake (solid line) and the exhaust (dashed line) valve timing. To increase the amount of fresh air in the cylinder, the intake valve timing was shifted from  $28^{\circ}\text{CAaTDC}$  toward TDC of the gas exchange ( $10^{\circ}\text{CAaTDC}$ ) while the exhaust valve timing remained unchanged within the first 11 cycles. In the following 10 cycles, the exhaust valve timing was shifted toward TDC to increase internal exhaust gas recirculation in a first step, which was further increased by a second shift starting with cycle 29. At the same time, the intake manifold pressure was increased from 0.33 to 0.95 bar, as shown in Figure 4(b). The resulting overall IMEP evolution is shown in Figure 4(c). The IMEP increases from about 1.1 to 4.7 bar. Since the turbulence intensity was reduced by the Miller cycle, the MFB50 was in the range of  $5\text{--}20^{\circ}\text{CAaTDC}$  despite adjusted spark timing, as shown in Figure 4(d). A total of 19 repetitions of the maneuver were performed. Since the engine parameters were in good agreement with those of the four-cylinder engine, the feasibility of the endoscopic test rig for realistic transient operation was demonstrated.<sup>24</sup> Furthermore, the low cycle-based standard deviation of the engine parameters (gray area in Figure 4) prove the good reproducibility of the maneuver. The higher standard deviations of the MFB50 were due to cycle-to-cycle variations in mixture preparation caused by the Miller cycle.

**Table 2.** Engine parameters of transient TOP and stationary operation point SOP.

	TOP	SOP
Intake manifold pressure in bar	0.53	0.53
IMEP in bar	3.84	3.77
MFB50 in $^{\circ}\text{CAaTDC}$	6.9	6.7

To investigate the differences of the in-cylinder processes, a transient operating point is compared with the corresponding stationary operating point. For this purpose, several consecutive cycles, referred to as the transient cycle range (TCR), were combined for statistical evaluation. The highest engine parameter gradients were observed from cycle 10 to 19, further referred to TCR1 (red area in Figure 4). Within cycle 20–28 referred to TCR2 (blue area in Figure 4), valve timing remained almost unchanged and smaller gradients in intake manifold pressure and IMEP existed. The average engine parameters of TCR1 (red dot) and TCR2 (blue dot), and of the corresponding stationary operating points SOP1 (red dashed line) and SOP2 (blue dashed line) are shown in Figure 4 and further specified in Table 3.

### Multi-parameter-diagnostics

Due to the limited optical accessibility of the full-metal engine, a multi-parameter endoscopic imaging approach was developed for the investigation of in-cylinder flow, flame propagation, and soot formation during transient engine operation. Figure 1 shows the experimental setup.

Endoscopic high-speed PIV was applied to investigate the flow field. The seeding particles used for PIV were illuminated by a laser sheet in the central symmetry plane. The laser sheet, 65 mm in height and  $\sim 330\ \mu\text{m}$  thick, was formed by passing the beam of a frequency doubled dual-cavity Nd:YVO<sub>4</sub> laser (Edgewave, 532 nm, 0.7 mJ/pulse) through two cylindrical lenses ( $f = -50\ \text{mm}$  and  $f = 700\ \text{mm}$ ) and the sapphire glass entrance window ( $f = -50\ \text{mm}$ ). The laser was aligned within the engine with the cylinder head removed. With the cylinder head reinstalled, the alignment was further checked using targets at the entrance window, the center of the combustion chamber, and the exit window. The dependency of light scattering on the polarization of the laser light was reduced by placing a quarter-wave plate in front of the laser exit.

The scattered light was detected using an endoscope specially designed for the combustion chamber geometry. The endoscope had a diameter of 12 mm and was mounted in the cylinder head between the intake and exhaust valves at an angle of  $27^{\circ}$  to the horizontal plane. The endoscope was equipped with a beam

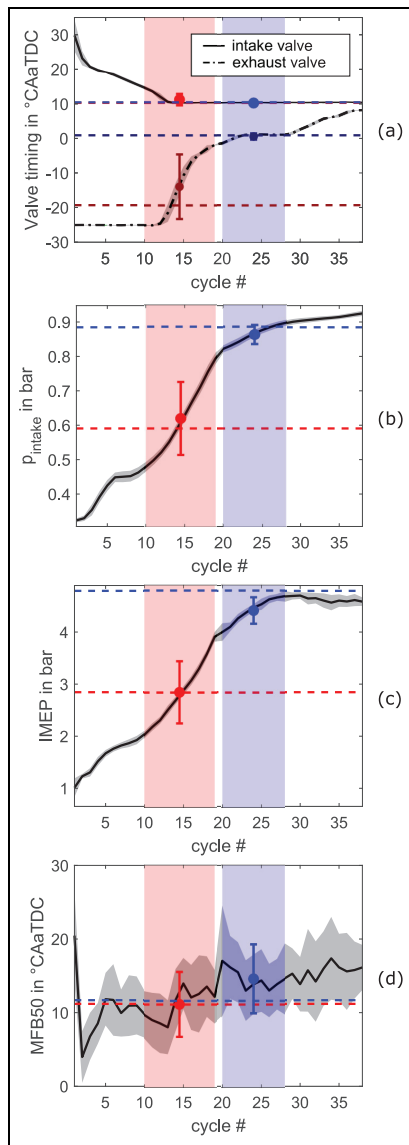


**Figure 4.** Valve timing of intake valve opening indicated by the solid line and exhaust valve closing indicated by the dashed line: (a) intake manifold pressure, (b) indicated mean effect pressure IMEP, (c) 50% mass fraction burned MFB50, and (d) along the cycles of the tip-in. Black lines indicate phase-average and gray area indicates one standard deviation. The average of TCR1 and TCR2 (rectangle) is indicated by the red and blue dots, and the average of SOP1 and SOP2 by the red and blue dashed lines.

splitter that reflected light in the wavelength range of  $540\text{ nm} \pm 60\text{ nm}$  with a reflectivity of 90% toward the PIV-camera (Phantom v1611). The remaining light in the range of 300 to 1000 nm was transmitted toward the VIS-camera (Phantom v1611, color). Both cameras were focused on the central symmetry plane using a Scheimpflug arrangement. The field-of-view for PIV was an ellipsoid 79 mm in height and 70 mm in width given by the combination of the viewing cone angle of  $74^\circ$  and the central symmetry plane. The PIV measurements were conducted at a frame rate of 5.6 kHz, resulting in a temporal resolution of  $1.5^\circ\text{CA}$  at 1400 rpm. For the investigation of flame propagation and soot

**Table 3.** Engine parameters of the transient cycle ranges TCR1 and TCR2 and the corresponding stationary operating points SOP1 and SOP2.

	TCR1	SOP1	TCR2	SOP2
Intake manifold pressure in bar	0.62	0.59	0.86	0.88
IMEP in bar	2.85	2.85	4.41	4.79
MFB50 in °CAaTDC	11.2	11.2	14.7	11.7

formation, the VIS-camera was operated at 11.2 kHz, resulting in a temporal resolution of  $0.75^\circ\text{CA}$  at 1400 rpm. The exposure time was set to  $70\ \mu\text{s}$  for flame imaging. Early flame chemiluminescence is characterized by emissions from exited radicals in a wavelength range of 300 to 450 nm and when soot is formed the luminosity increases especially at higher wavelengths.<sup>25</sup> The combination of the beam splitter and quantum efficiency of the VIS-camera allowed the detection of emissions within a range of about 400 to 650 nm.

Endoscopic imaging for PIV can lead to a perspective error, which is described in more detail in Dierksheide et al.,<sup>23</sup> Reeves and Lawson<sup>26</sup> and Adrian.<sup>27</sup> The error can be reduced by applying stereoscopic imaging,<sup>26</sup> which was not feasible within this engine. To avoid relative motion of the endoscope, cameras, and engine due to engine displacement during transients and engine vibrations, the components were firmly connected to each other.

### Processing

**PIV processing.** A commercial software DaVis 8.4.3 (LaVision) was used for PIV processing. The distortion was corrected using imaging of a calibration target and a pinhole camera model which was most suited due to the angle of the optical axis to the horizontal plane.<sup>28,29</sup> To position the target inside the combustion chamber at the central symmetry plane, the cylinder head, and endoscope had to be disassembled and reassembled, with locating pins ensuring reproducible positioning of the components. The position was verified using the spark plug in the images. A linear shift was performed before the distortion correction, if there was a shift of individual pixels between the target image and the current measurement. To increase image contrast, the minimum intensity of each pixel of all cycles was subtracted from the raw particle images for each crank angle. For each image, the moving average was subtracted with a filter length of 12 pixels and the intensity was normalized with a filter length of 16 pixels. The multi-pass cross-correlation algorithm was applied with decreasing interrogation window size from  $64 \times 64$  pixels to  $32 \times 32$  pixels in three iterations and a window overlap of 75%. The resulting mean vector spacing was about 1.0 mm. Vectors with a peak ratio of  $< 1.8$  were

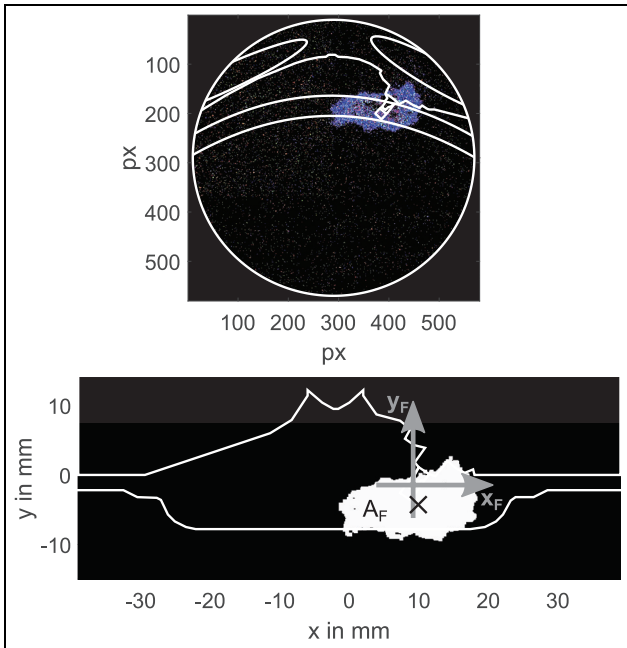


**Figure 5.** Single flame image: raw color image (top), processed flame image (bottom) with flame area  $A_F$  and its centroid (cross).

designated as spurious vectors, which were iteratively removed using a two-times median filter including a  $3 \times 3$  smoothing operation.

**Flame imaging processing.** Figure 5 shows a raw image of an early flame kernel (top). For orientation, contours of the valves, cylinder head including the gap of the injector, and the spark plug are shown, as well as the outer and inner contour of the piston top land. The contour of the piston top land was adapted for each crank angle. The flame images considered were in a phase of the cycle, at which the piston was in front of the laser entrance windows. Therefore, no laser light was visible in the images. For flame imaging, only the blue channel of the VIS-camera was evaluated, with the intensities resulting from interpolation of the Bayer sensor. A distortion correction was applied according to PIV processing. Flame contour extraction was applied similar to other investigations.<sup>21,30,31</sup> The maximum of the sensor noise was estimated in a region without flame intensities and used as a threshold. A maximum filter with a filter length of five pixel was used to reduce the sensor noise, and then the threshold was applied for binarization. Areas smaller than 50 pixels were eliminated. The flame area  $A_F$  was then given by the number of pixels within the remaining area. The uncertainty of  $A_F$  was about 1–2 pixel along the flame contour due to the uncertainty in pixel assignment to the flame contour using the maximum filter. In addition, the coordinates  $x_F$  and  $y_F$  of the flame area centroid relative to the center of the spark plug gap were determined as shown by the cross in Figure 5 (bottom).

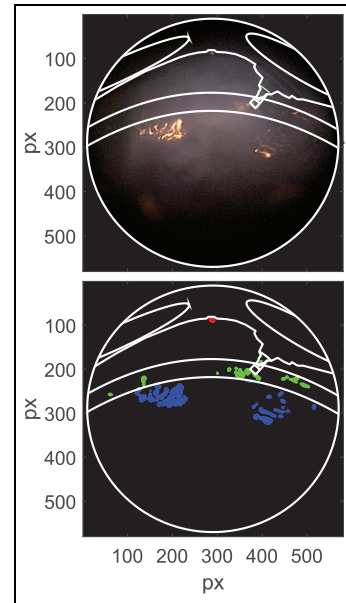


**Figure 6.** Individual combustion image at MFB90: raw color image (top), processed image (bottom) with soot particle areas: pool fire  $A_p$  (blue area), crevice  $A_p$  (green area) and injector  $A_p$  (red area).

**Soot processing.** Figure 6 shows a raw image during late combustion with soot formation (top). The images were evaluated at 90% mass fraction burned MFB90, since preliminary studies revealed a good correlation between MFB90 and particle number emission measured in the exhaust. White balance was applied to the VIS-camera images with a calibration image illuminated via white LEDs. The extracted soot measurements were not quantitative and hence no spectral calibration was needed. The combustion emission spectrum consists of chemiluminescence from the reaction zone and black-body radiation from the soot luminosity, which are dominant in different wavelength ranges.<sup>25</sup> Due to the spectral overlap of the three color channels, part of the emissions from chemiluminescence in the late combustion phase was detected by the red channel. Therefore, the intensities of the blue channel were pixelwise subtracted from the red channel, limiting the difference to 255 counts. Then, the peak signal-to-noise ratio was increased using a block matching 3D (BM3D)-filter by Dabov et al.<sup>32</sup> Furthermore, an average filter with a filter length of 25 pixel normalized the gas phase intensities and accentuated the contour of the soot areas. The maximum pixel value of a processed cycle, which showed only soot in the gas phase, was used as the threshold for binarization. The sum of the pixels is further referred to as the soot particle area  $A_p$ . In order to investigate soot formation from different sources or locations of the combustion chamber, the pixels were referenced to specific regions based on the combustion chamber contours. Figure 6 (bottom) shows the processed combustion image. The sum of pixels within a

**Table 4.** Number of cycles  $N$  and correlation value thresholds  $R_c$  for a significance of 1% for each operating point and cycle range.

	$N$	$R_c$
Load step		
TOP	47	0.37
SOP	272	0.16
Tip-in		
TCR1	190	0.19
SOP1	300	0.15
TCR2	171	0.20
SOP2	300	0.15

field of  $50 \times 160$  pixels below the injector was caused by tip sooting and was referred to the injector  $A_p$  (red area). Between the lower piston contour and up to 20 pixels above the upper piston contour, the sum of pixels was referred to the crevice  $A_p$  (green area). The sum of pixels below the lower piston contour was due to pool fire and was therefore referred to pool fire  $A_p$  (blue area).

Due to the endoscopic imaging, the soot luminosity near the endoscopic access appears brighter and larger in space than the corresponding luminosity at the other end of the combustion chamber. The intensity variations were compensated for by the processing. The uncertainty in the area could not be corrected within this work. Since the start of injection remained unchanged within the two maneuvers, the interactions of the fuel with the wall led to fuel films at roughly the same positions. Hence, the soot particle areas and their variations were comparable within each maneuver.

**Correlation maps.** The correlations between the flow field and early flame propagation, as well as the flow field and soot particle areas were investigated using a statistical analysis. The method was introduced by Stiehl et al.<sup>33</sup> and revised by Bode et al.<sup>12</sup> For a given crank angle, the Pearson correlation coefficient  $R$ <sup>12</sup> was evaluated for one component of each velocity vector and one parameter of the flame or soot particle area, respectively. The correlation map was obtained from the correlation coefficients of all vectors of the flow field. Furthermore, a two-sided statistical  $t$ -test<sup>12</sup> was applied. The  $H_0$ -hypothesis was the statistical independence of both quantities. The sample size was given by the total number of cycles  $N$ . For a significance of 1%, the test quantities and correlation value threshold  $R_c$  were calculated for each operating point and cycle range of the transient maneuver studied. Table 4 lists the corresponding  $N$  and  $R_c$ . For  $R$  greater than  $R_c$ , the quantities were assumed to be correlated as the  $H_0$ -hypothesis was rejected. Within the correlation maps, these  $R$  values are shown according to the color map. Flow regions with  $R$  below  $R_c$  are shown in white color and refer to uncorrelated quantities.

## Results

In order to investigate the interactions between the in-cylinder processes, a statistical analysis of the simultaneous multiparameter measurements is performed in the following. By comparing the transient and steady-state operating points, the effect of transient operation on the processes in the cylinder is analyzed.

### In-cylinder flow

For the investigation of the in-cylinder flow during the transients, the phase-averaged flow fields of the stationary operating points were compared to those of the corresponding transient operating point during the load step or the transient cycle ranges during the tip-in. The phase-averaged flow fields were calculated for the number of cycles given in Table 4. Although, the number of cycles was not the same, the average converged and was thus sufficient for comparison. The phase-averaged flow fields are shown together with the contours of the cylinder head, piston and intake valves for orientation. The intake valves also covered a part of the combustion chamber which is masked by an ellipse (black face and gray outline). The lengths of the vectors are normalized to their velocity magnitudes, which are shown by the color map.

**Load step.** The formation of the characteristic tumble flow begins during the intake stroke with the opening of the intake valve and the valve lift being symmetric. The flow over the intake valves depends on the pressure difference over the valves resulting from the moving piston and hence the engine speed and valve timing. This flow is reflected by the cylinder wall and the piston. The flow thereupon begins to circulate and the circulation enhances during the compression stroke resulting in a tumble flow. In contrast to the stationary operating point SOP, the transient operating point TOP was characterized by an intake manifold pressure that increased over the investigated cycle. The influence of the pressure increase on the flow field of TOP is further investigated. Figure 7 shows the phase-averaged flow fields of the transient operating point TOP (left) and stationary operating point SOP (right). At  $-268^\circ\text{CAaTDC}$  (top), the flow fields above  $y = -30$  mm were in good agreement. This also holds for the flow fields at  $-91^\circ\text{CAaTDC}$  (middle), where, in particular, the tumble centers nearly coincided. In the area below  $y = -30$  mm (white rectangle), differences in velocity magnitude were visible as well as in the vector direction at both crank angles shown. The differences were attributed to variations in seeding density during the transient, so that the reflections from the piston could not be completely reduced by the PIV processing described in the processing section. Especially, the contrast enhancement using the minimum subtraction varied with the varying seeding density. As the piston moved upward during compression, the influence

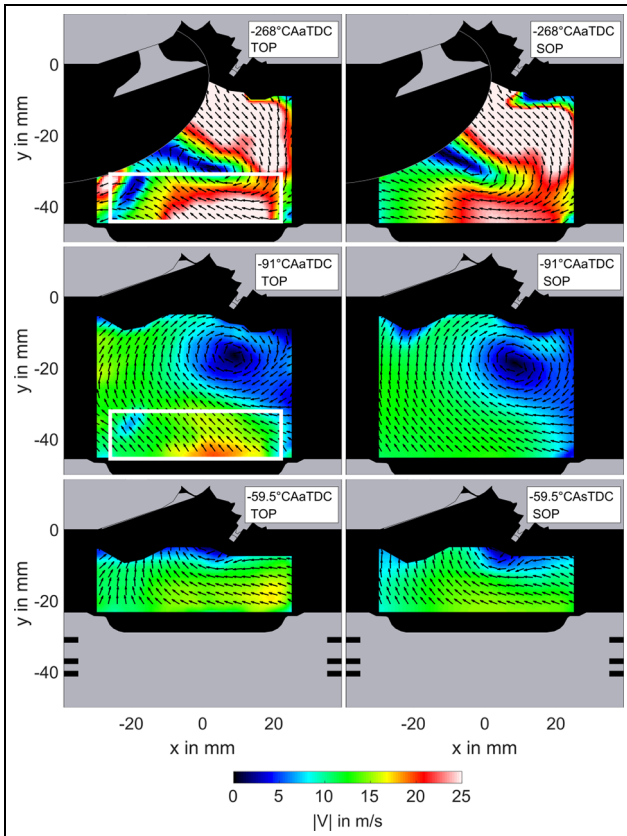


**Figure 7.** Phase-averaged flow fields of the transient operating point TOP (left) and stationary operating point SOP (right) at  $-268^\circ\text{CAaTDC}$  (top),  $-91^\circ\text{CAaTDC}$  (middle) and  $-59.5^\circ\text{CAaTDC}$  (bottom). Length of each vector is normalized by its magnitude and the velocity magnitudes are shown according to the color bar.

decreased. At  $-59.5^\circ\text{CAaTDC}$  (bottom), the flow field of TOP showed no evidence of reflections off the piston. For TOP and SOP, the tumble center moved toward the symmetry axis. Both flow fields were in good agreement in terms of velocity magnitudes and flow directions. Since there was no significant difference in the flow fields at either crank angle, it can be assumed that there was no significant influence of the intake manifold pressure increase on the in-cylinder flow.

**Tip-in.** During tip-in, in addition to the intake manifold pressure rise, the valve timing changes. Furthermore, the applied Miller cycle will change the in-cylinder flow. Variations in valve timing result in varying piston speeds relative to valve lift, as well as intake and exhaust manifold pressure oscillations that result in varying internal exhaust gas recirculation. With respect to the Miller cycle, the early intake valve closing decreases the flows kinetic energy. This is to be counteracted by asymmetric intake valve lifts, which should store kinetic energy in a mixed tumble and swirl motion to reduce energy dissipation during the further compression stroke after early intake valve closing.

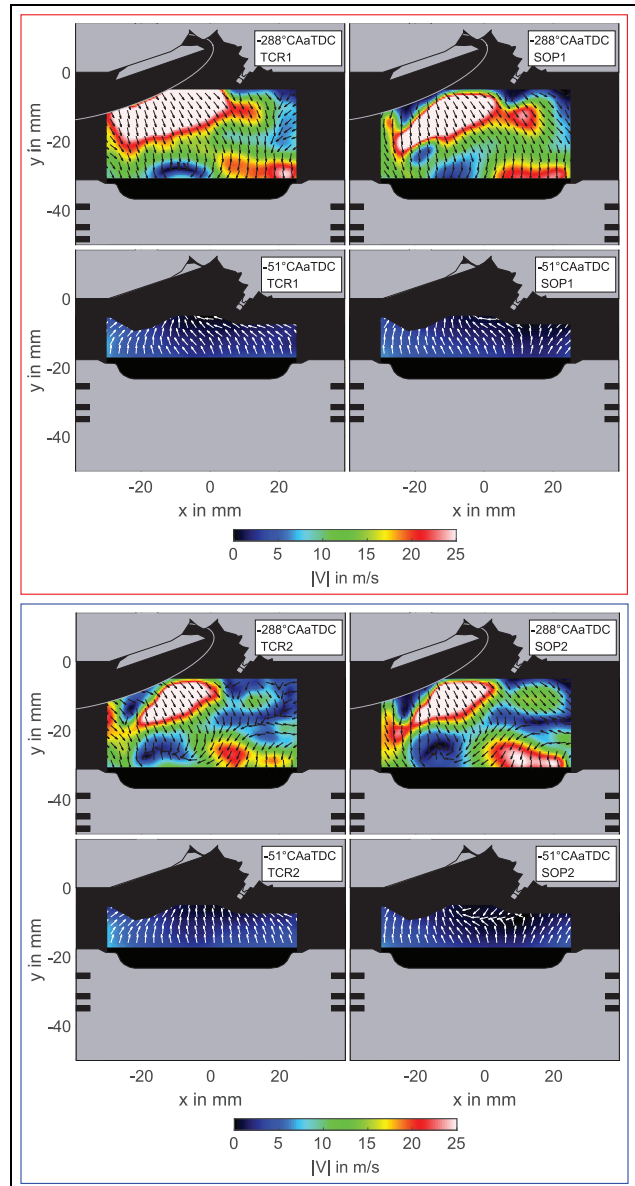


**Figure 8.** Phase-averaged flow fields of cycle ranges during tip-in and stationary operating points. Red rectangle: transient cycle range TCR1 (left) and stationary operating point SOP1 (right) at about  $-288^\circ\text{CAaTDC}$  (top) and  $-51^\circ\text{CAaTDC}$  (bottom). Blue rectangle: transient cycle range TCR2 (left) and stationary operating point SOP2 (right) at about  $-288^\circ\text{CAaTDC}$  (top) and  $-51^\circ\text{CAaTDC}$  (bottom). Length of each vector is normalized by its magnitude and the velocity magnitudes are shown according to the color bar.

However, no structured in-cylinder flow was observed within this investigation.

Figure 8 shows phase-averaged flow fields of transient cycle ranges during tip-in and the corresponding stationary operating points. The asymmetric valve lifts resulted in a combination of tumble and swirl motion. The interaction of the different asymmetric flows reduced the flows kinetic energy. Hence, the flow velocity was reduced and no tumble flow was formed during the compression stroke. Within the red rectangle at



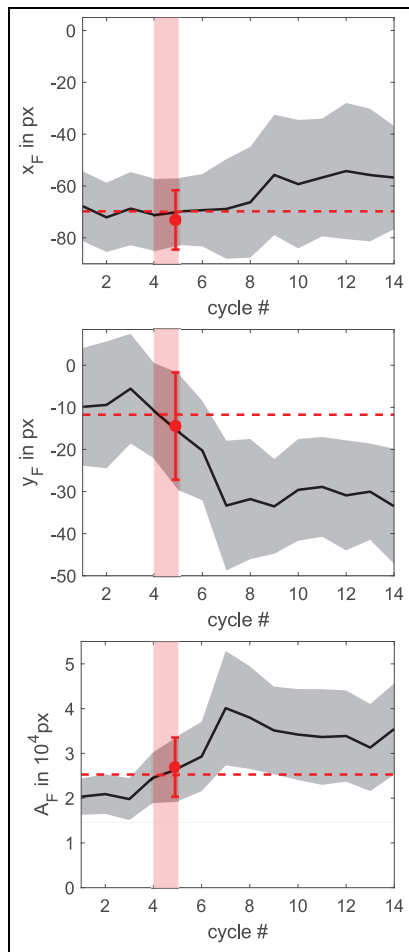


**Figure 9.** Evolution of the extracted flame parameters at 10°CAaTOI along the cycles of the load step: centroid coordinates  $x_F$  (top) and  $y_F$  (middle) and the flame area  $A_F$  (bottom). Black lines indicate the phase-average and the gray area one standard deviation. The average of TOP (red rectangle) is indicated by the dot and the average of SOP by the dashed line.

–288°CAaTDC, the flow fields of TCR1 and SOP1 show high velocity magnitudes below the intake valves and above the piston for  $x > 0$  mm, where the flow was directed toward the piston surface. Weak velocity magnitudes were visible above the piston for  $-20$  mm  $< x < 0$  mm at TCR1 and SOP1. Whereat, these regions of weak velocity could have high velocity out of plane components. At –51°CAaTDC, the in-cylinder flow was directed upwards with velocity magnitudes well below 10 m/s. Differences in flow direction were visible in the right half of the flow fields. Within the blue rectangle of Figure 8, the phase-averaged flow fields of TCR2 and SOP2 are shown. At –288°CAaTDC, delayed exhaust valve closing led to decreased velocity magnitudes in the regions below the intake valves and the spark plug. Above the piston, the flow fields at the right side were directed more strongly toward the symmetry axis of the cylinder and larger regions with small velocity magnitudes were found on the left side. At

–51°CAaTDC, the flow fields were similar to those of TCR1 and SOP1. The overall flow structures were in a good agreement. Differences were found at the left and right edges of the flow fields. All differences between the transient cycle ranges and the stationary operating points were in the same range as the standard deviation and uncertainty of the velocity magnitudes. The differences between TCR1 and TCR2 or SOP1 and SOP2, which were due to a variation in exhaust valve timing and thus an increase in internal exhaust gas recirculation, were found to be significant. In contrast to the load step, no tumble flow was formed during the tip-in due to the asymmetric valve lifts and Miller cycle.

### Flame propagation

**Load step.** Figure 9 shows the evolution of the extracted flame parameters 10°CA after start of ignition (aTOI) along the cycles of the load step. The flame, supported by the directed in-cylinder flow, propagated toward the cylinder symmetry axis for all cycles along the load step, as indicated by the phase-averaged horizontal position of the flame area centroid  $x_F$  (top). As the load increased, the flame propagated more toward the piston, as indicated by the evolution of the phase-averaged  $y_F$  (middle). The phase-averaged flame area  $A_F$  (bottom) increased continuously from cycle 1 to 7 and continued to remain unchanged within the range of the standard deviation for subsequent cycles. Thus, the flame area increased with increasing load which explains the adaption of the start of ignition to keep MFB50 constant during the load step. The comparison of TOP (red dot) and SOP (red dashed line) showed good agreement in the phase-averaged extracted flame parameters, and no influence of the intake pressure manifold gradient on flame propagation was found.

**Tip-in.** Figure 10 shows the evolution of the extracted flame parameters at 20°CAaTOI along the cycles of the tip-in. Up to cycle 10, the flame propagates toward the exhaust valves, as indicated by the phase-averaged  $x_F$  (top). Since the flow was not directed, the flame propagation was slow and in all directions. As the tip-in progressed, the flame propagation fluctuated around the spark plug gap position, as indicated by the high standard deviation, making an interpretation difficult. As load increased, the flame propagated less toward the piston, as indicated by the phase averaged  $y_F$  (middle). This is in contrast to the flame propagation during the load step. A reason could be the different structures of the flow fields. Furthermore, the phase-averaged flame area  $A_F$  (bottom) does not show a clear evolution along the cycles of the tip-in. The phase-averaged flame parameters of TCR1 (red rectangle) and SOP1 (red dot), or those of TCR2 (blue rectangle) and SOP2 (blue dot), were in good agreement.

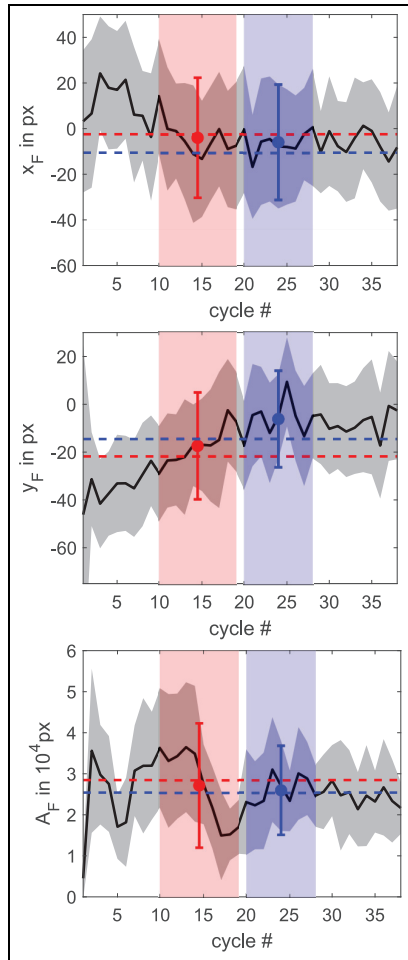


**Figure 10.** Evolution of the extracted flame parameters at 20°C AaTOI along the cycles of the tip-in: centroid coordinates  $x_F$  (top) and  $y_F$  (middle) and the flame area  $A_F$  (bottom). Black lines indicate the phase-average and the gray area one standard deviation. The average of TCR1 and TCR2 (rectangle) are indicated by the red and blue dots, and the average of SOP1 and SOP2 by the red and blue dashed lines.

### Soot formation

**Load step.** Figure 11 shows the evolution of the different soot particle areas  $A_P$  along the cycles of the load step. All three phase-averaged  $A_P$  (black lines) increased with the onset of the load step and remained constant within the standard deviations. The injector  $A_P$  (top) was the lowest in value and fluctuations, the latter indicated by the standard deviation (gray area). The crevice  $A_P$  (middle) was about three times higher than pool fire  $A_P$  (bottom), but had equally high fluctuations. The increase of  $A_P$ , especially of pool fire  $A_P$ , with increasing load could be due to the surface temperatures. Comparing the phase-averaged  $A_P$  of TOP (red dot) and SOP (dashed line), higher phase-averaged crevice  $A_P$  were found for TOP. As the load increases during the transient, the surface temperature was assumed to be lower than at the corresponding stationary operating point because the time required for the load increase was shorter than that required for the surface

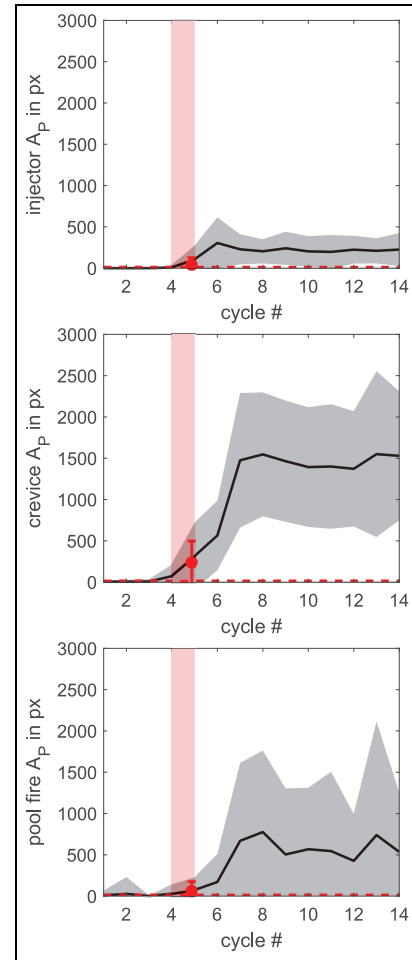


**Figure 11.** Evolution of injector  $A_P$  (top), crevice  $A_P$  (middle), and pool fire  $A_P$  (bottom) along the cycles of the load step. Black lines indicate the phase-average and the gray area one standard deviation. The average of TOP (rectangle) is indicated by the dot and the average of SOP by the dashed line.

temperature increase, which is in the order of minutes.<sup>4</sup> The formation of pool fire could be further supported by the increasing flame area and the lower position of the flame area centroid, which reduces the time available for wall film vaporization. The direct comparison shows a clear difference between TOP and SOP. While the soot particle areas for the steady-state operating point are almost zero, the transient operating point leads to a significant increase.

**Tip-in.** Figure 12 shows the evolution of the different soot particle areas  $A_P$  along the cycles of the tip-in. Similar to the load step, the phase-averaged (black line) injector  $A_P$  (top) increased with increasing load. In contrast to the load step, the phase-averaged pool fire  $A_P$  (bottom) was higher than the phase-averaged crevice  $A_P$  (middle) and both showed no systematic evolution during the tip-in. The comparison of the transient cycle ranges with the stationary operating point did not reveal any differences with respect to  $A_P$ . One reason could be the early  $\text{SOI} = -290^\circ\text{CAaTDC}$  in

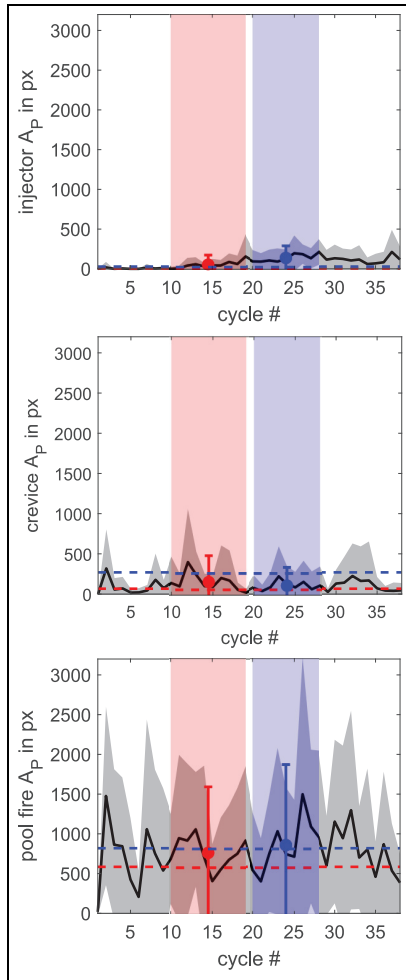


**Figure 12.** Evolution of injector  $A_P$  (top), crevice  $A_P$  (middle) and pool fire  $A_P$  (bottom) along the cycles of the tip-in. Black lines indicate the phase-average and the gray area one standard deviation. The average of TCR1 and TCR2 (rectangle) are indicated by the red and blue dots, and the average of SOP1 and SOP2 by the red and blue dashed lines.

combination with the inefficient mixture formation due to the low flow velocities caused by the applied Miller strategy in the transient and stationary operating points.

**Correlation analysis**

The soot particle areas are subject to high cycle-to-cycle and transient-to-transient variations. The simultaneous measurement approach enabled correlation analyses to further analyze cause-and-effect chains during the transients and the corresponding stationary operating points.

**Load step.** During the load step, correlation analysis was used to reveal relations between the flow field and the flame parameters shortly after ignition and the soot particle area of pool fire, respectively. Figure 13 schematically shows the relationship between the horizontal

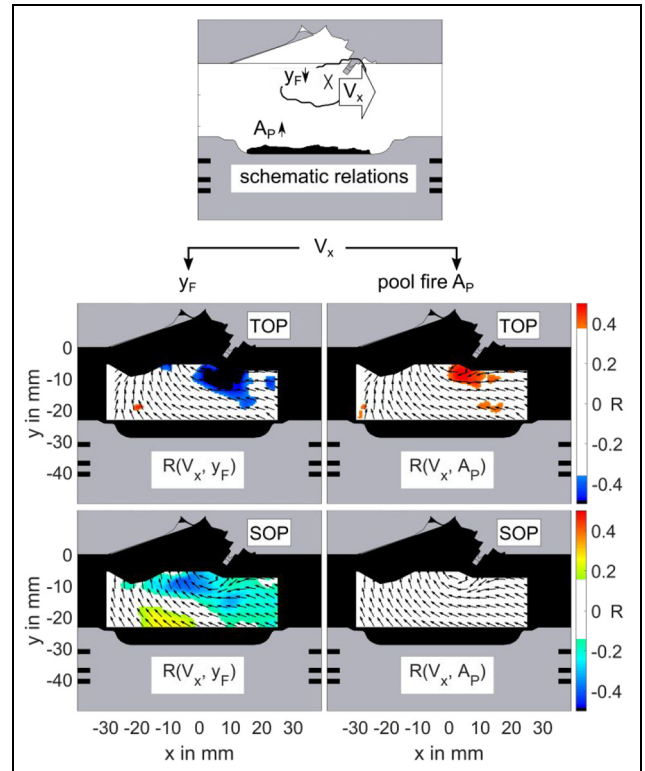


**Figure 13.** Schematic relations (top) of  $V_x$ ,  $y_F$ , and pool fire  $A_P$ . Correlation maps of  $V_x$  with  $y_F$  (left) and pool fire  $A_P$  (right) at TOP (middle) and SOP (bottom). Correlation coefficients are shown according to the color bars.

velocity component  $V_x$ , the vertical flame area centroid coordinate  $y_F$  and pool fire  $A_P$  (top) and exemplarily the corresponding correlation fields of the flow field at  $-59.5^\circ\text{CAaTDC}$ , the flame parameters at  $10^\circ\text{CAaTOI}$  and the soot particle area (middle and bottom). For TOP (middle), the correlation map of  $V_x$  with  $y_F$  (left) shows a significant negative correlation in the region below the spark plug, while in the same region, the correlation map of  $V_x$  with pool fire  $A_P$  (right) shows a significant positive correlation. Figure 13 (bottom) shows the correlation maps for SOP. Although a significant negative correlation of  $V_x$  with  $y_F$  (left) was found over a wide region of the flow field, the correlation coefficients of  $V_x$  with pool fire  $A_P$  (right) were not significant. Figure 14 shows the correlation between the vertical velocity component  $V_y$ , the vertical flame area centroid coordinate  $y_F$  and pool fire  $A_P$ . For TOP (middle) and SOP (bottom), the correlation coefficients of  $V_y$  with  $y_F$  (left) above the piston and around the symmetric axis were significant positive (bottom). Again, only for TOP significant correlation coefficients of  $V_y$  with pool fire  $A_P$  (right) were found in about the same region. That is, when the horizontal component of the flow  $V_x$  is less pronounced to the left and/or the vertical velocity component  $V_y$  is less pronounced to the top, the flame hits the piston earlier resulting in a higher pool fire probability increasing  $A_P$ . This is indicative of wall wetting of the piston, with which the

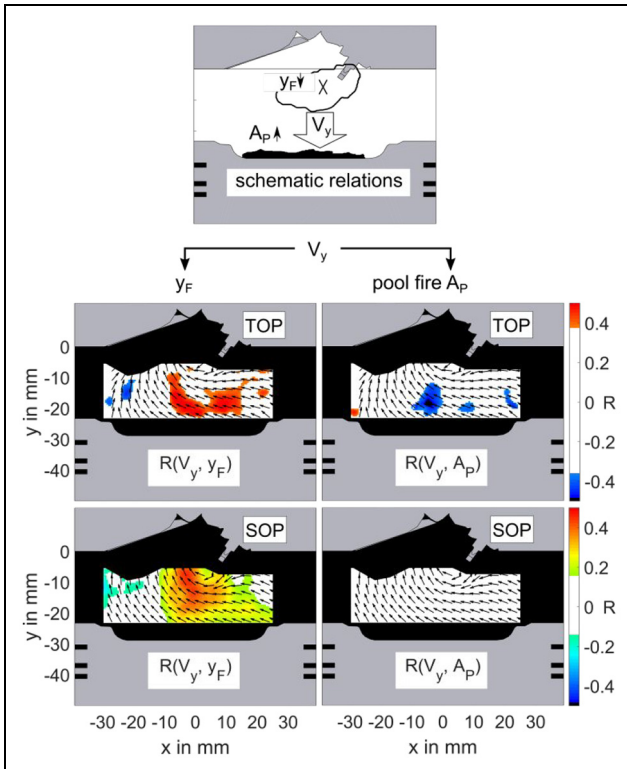


**Figure 14.** Schematic relations (top) of  $V_y$ ,  $y_F$ , and pool fire  $A_P$ . Correlation maps of  $V_y$  with  $y_F$  (left) and pool fire  $A_P$  (right) at TOP (middle) and SOP (bottom). Correlation coefficients are shown according to the color bars.

earlier impingement of the flame has less time available for evaporation and mixing, resulting in a more pronounced sooty diffusion flame.

**Tip-in.** For the tip-in, the correlation analysis showed similar relations as for the load step. Figure 15 shows the correlation analysis maps for the flow field at  $-51^\circ\text{CAaTDC}$ , the flame parameters at  $25^\circ\text{CAaTOI}$  and the soot particle area of pool fire  $A_P$  for TCR1 and SOP1 (red rectangle) and TCR2 and SOP2 (blue rectangle), respectively. For TCR1 (middle), the correlation map of  $V_x$  with  $y_F$  (left) shows a significant positive correlation in the region above the piston which coincides with the area of significant negative correlation of  $V_x$  with pool fire  $A_P$  (right). About the same correlations are observed within the correlation maps of SOP1 (bottom). For TCR2 and SOP2 significant correlation of  $V_y$  were found instead of  $V_x$ .  $V_y$  correlated significantly positive with  $y_F$  (left) in the region between the spark plug and the piston. For TCR2, there were also positive significant correlation coefficients above the piston left of the symmetry axis. Within these regions,  $V_y$  correlated significantly negatively with pool fire  $A_P$  (right). Similar correlations were observed for the steady-state operating points SOP1 and SOP2, shifting somewhat

with respect to the region in the flow field, which may be due to changes in the three-dimensional flow in the cylinder caused by changes in valve timing, although no significant differences were found in the phase-averaged flow fields between the stationary operating points and the tip-in.

A correlation analysis of soot formation at the injector tip is shown in Figure 16 for the flame parameters at  $20^\circ\text{CAaTOI}$  and the velocity component  $V_y$  at  $-51^\circ\text{CAaTDC}$  for TCR1 and SOP1 (red rectangle) and TCR2 and SOP2 (blue rectangle). In all cases,  $V_y$  correlates with  $y_F$  in the region below the spark plug (left columns). The positive correlation coefficients of  $V_y$  with injector  $A_P$  (right columns) were in approximately the same regions for TCR1 and TCR2. This means that the flame hits the injector earlier with a stronger upward flow, which in turn promotes soot formation at the injector, as already shown for pool fire  $A_P$ . In the stationary cases SOP1 and SOP2, no soot formation was observed at the injector.

In summary, the correlation analysis revealed relations between the flow field during late compression and the flame propagation toward the related source of soot formation. Significant correlations of the velocity component with the respective flame area centroid component were found in the transient operating cycles during the load step and the tip-in, as well as the corresponding stationary operating points. Significant correlations of the flow field component with the pool fire  $A_P$ , on the other hand, were only observed during the transient operating point of the load step. Similarly, correlations with respect to the injector  $A_P$  were only observed during the transient cycle ranges of the tip-in.

## Conclusion

Simultaneous endoscopic PIV and combustion visualization were applied to a single-cylinder DISI engine. The endoscopic full metal engine and test rig modification allowed the investigation of in-cylinder flow, flame propagation, and soot formation during real transient maneuvers. The reproducible application of a generic load step and a realistic tip-in with Miller cycle allowed statistical analysis. Parameters were extracted from the flow field, the flame propagation, and the formation of soot from different sources.

The comparison of transient and stationary operation showed no difference in the phase-averaged flow fields within the measurement uncertainty. The evolution of flame area and vertical flame propagation were contrary along the cycles of the load step and the tip-in. By analyzing the different soot sources, differences in the evolution were found during load step and tip-in. The detected area of soot luminosity  $A_P$  related to pool fire and respectively crevice increased with load during the load step, but remained almost unchanged during

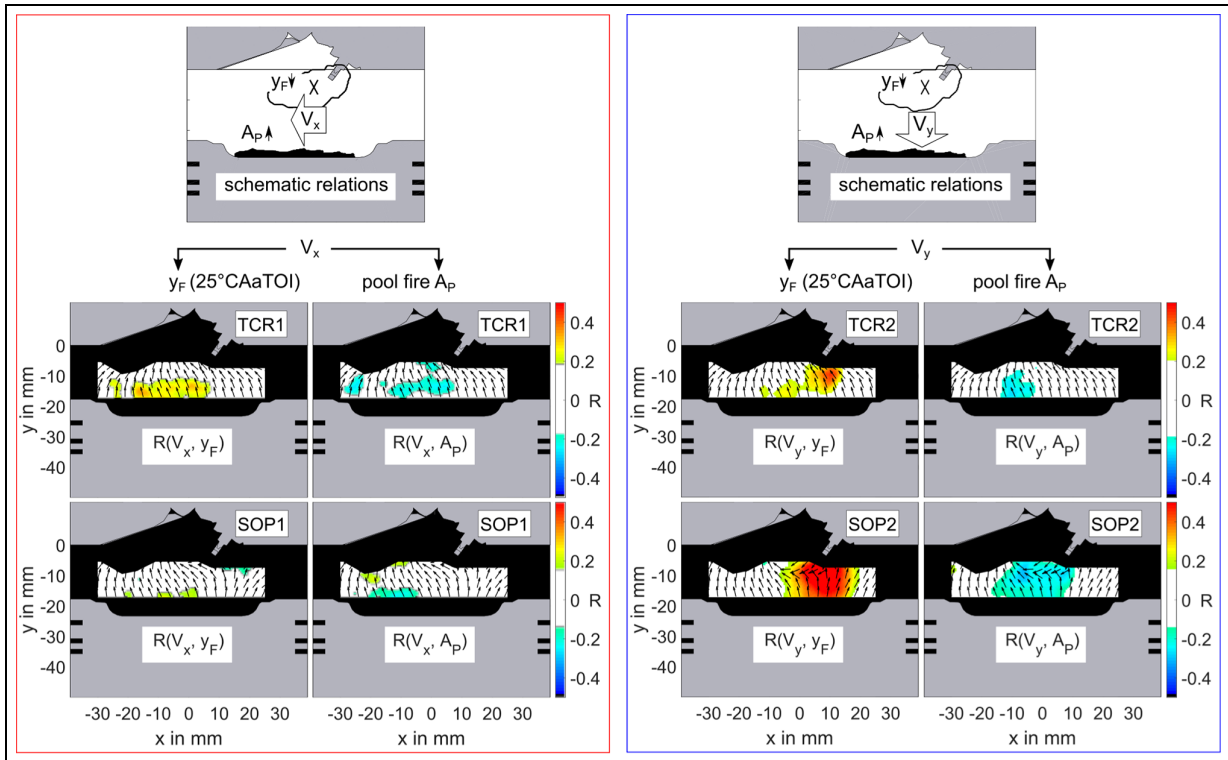


**Figure 15.** Red rectangle: Schematic relations (top) of  $V_x$ ,  $y_F$ , and pool fire  $A_p$ . Correlation maps of  $V_x$  with  $y_F$  (left) and pool fire  $A_p$  (right) at TCR1 (middle) and SOP1 (bottom). Blue rectangle: Schematic relations (top) of  $V_y$ ,  $y_F$ , and pool fire  $A_p$ . Correlation maps of  $V_y$  with  $y_F$  (left) and pool fire  $A_p$  (right) at TCR2 (middle) and SOP2 (bottom). Correlation coefficients are shown according to the color bars.

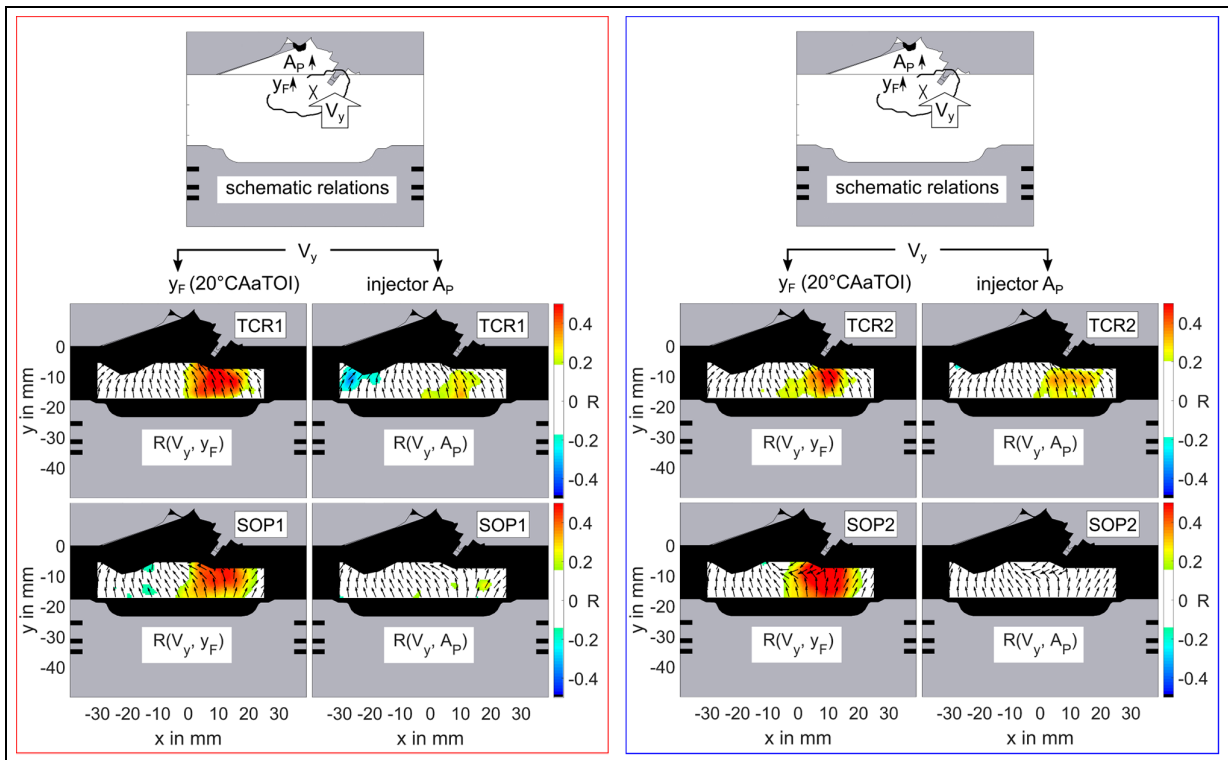


**Figure 16.** Red rectangle: Schematic relations (top) of  $V_y$ ,  $y_F$  and injector  $A_p$ . Correlation maps of  $V_y$  with  $y_F$  (left) and injector  $A_p$  (right) at TCR1 (middle) and SOP1 (bottom). Blue rectangle: Schematic relations (top) of  $V_y$ ,  $y_F$ , and injector  $A_p$ . Correlation maps of  $V_y$  with  $y_F$  (left) and injector  $A_p$  (right) at TCR2 (middle) and SOP2 (bottom). Correlation coefficients are shown according to the color bars.

the tip-in. In contrast, injector  $A_P$  increased with load during both transients. Flow field, flame propagation, and soot formation underlie high variations.

The cycle-to-cycle and transient-to-transient variations in soot formation were assessed in more detail using correlation maps, indicating cause-and-effect chains of the flow field to soot formation. The common relations are: the flow field within specific regions causes the flame to propagate toward the combustion chamber surfaces where fuel films are likely to form, and the early arrival of the flame enhances soot formation. The observability of some of these cause-and-effect chains was only given by performing the transient engine operation. This indicates the importance of investigating and engine parameterization of transients with respect to soot formation.


### Declaration of conflicting interests

The author(s) declared no potential conflicts of interest with respect to the research, authorship, and/or publication of this article.

### Funding

The author(s) disclosed receipt of the following financial support for the research, authorship, and/or publication of this article: C. Fach and B. Böhm kindly acknowledge generous support by Deutsche Forschungsgemeinschaft through SFB-Transregio 150 project number 237267381-TRR150. A. Dreizler is grateful for generous support by the Gottfried Wilhelm Leibniz program of the Deutsche Forschungsgemeinschaft.

### ORCID iD

Christian Fach  <https://orcid.org/0000-0001-7279-3298>

### References

1. European Commission Regulation No 459/2012. *J Eur Union* 2012; 16–24.
2. European Commission Regulation 2017/1151. *J Eur Union* 2017; 1–643.
3. Boulouchos K and Kirchen P. A phenomenological mean value soot model for transient engine operation. *MTZ Worldw* 2008; 69: 58–65.
4. Peckham MS, Finch A, Campbell B, Price P and Davies MT. Study of particle number emissions from a turbocharged gasoline direct injection (GDI) engine including data from a fast-response particle size spectrometer. SAE technical paper 2011-01-1224, 2011.
5. Peckham MS, Finch A and Campbell B. Analysis of transient HC, CO, NO<sub>x</sub> and CO<sub>2</sub> emissions from a GDI engine using fast response gas analyzers. SAE technical paper 2011-01-1227, 2011.
6. Sabathil D, Koenigstein A, Schaffner P, Fritzsche J and Doehler A. The influence of DISI engine operating parameters on particle number emissions. SAE technical paper 2011-01-0143, 2011.
7. Hadler J, Lensch-Franzen C, Gohl M and Mink T. Einflussfaktoren auf die Partikelentstehung unter Realfahrbedingungen. *MTZ Motortech Z* 2016; 77: 52–61.
8. Drake MC, Fansler TD, Solomon AS and Szekely Jr GA. Piston fuel films as a source of smoke and hydrocarbon emissions from a wall-controlled spark-ignited direct-injection engine. SAE technical paper 2003-01-0547, 2003.
9. Ketterer JE and Cheng WK. On the nature of particulate emissions from DISI engines at cold-fast-idle. *SAE Int J Engines* 2014; 7: 986–994.
10. Stevens E and Steeper R. Piston wetting in an optical DISI engine: fuel films, pool fires, and soot generation. SAE technical paper 2001-01-1203, 2001.
11. Dageförde H, Kubach H, Koch T and Spicher U. Innermotorische Ursachen für Partikelemissionen bei Ottomotoren mit Direkteinspritzung. In: Bargende M, Reuss H-C and Wiedemann J (eds) *14. Internationales stuttgarter symposium*. Wiesbaden: Springer Fachmedien Wiesbaden, 2014, pp.435–459.
12. Bode J, Schorr J, Krüger C, Dreizler A and Böhm B. Influence of three-dimensional in-cylinder flows on cycle-to-cycle variations in a fired stratified DISI engine measured by time-resolved dual-plane PIV. *Proc Combust Inst* 2017; 36(3): 3477–3485.
13. Stiehl R, Schorr J, Krüger C, Dreizler A and Böhm B. In-cylinder flow and fuel spray interactions in a stratified spray-guided gasoline engine investigated by high-speed laser imaging techniques. *Flow Turbul Combust* 2013; 91: 431–450.
14. Peterson B, Reuss DL and Sick V. On the ignition and flame development in a spray-guided direct-injection spark-ignition engine. *Combust Flame* 2014; 161(1): 240–255.
15. Peterson B, Baum E, Böhm B and Dreizler A. Early flame propagation in a spark-ignition engine measured with quasi 4D-diagnostics. *Proc Combust Inst* 2015; 35(3): 3829–3837.
16. Baum E, Peterson B, Böhm B and Dreizler A. On the validation of LES applied to internal combustion engine flows: part I: comprehensive experimental database. *Flow Turbul Combust* 2014; 92(1–2): 269–297.
17. Nicollet F, Krüger C, Schorr J, Nicoud E, Colin O, Angelberger C, et al. A PIV-guided large-eddy simulation of in-cylinder flows. *Oil Gas Sci Technol Rev IFP Energies Nouv* 2017; 72(5): 28.
18. Steeper RR and Stevens EJ. Characterization of combustion, piston temperatures, fuel sprays, and fuel-air mixing in a DISI optical engine. SAE technical paper 2000-01-2900, 2000.
19. Kashdan J and Thirouard B. Optical engines as representative tools in the development of new combustion engine concepts. *Oil Gas Sci Technol Rev IFP Energies Nouv* 2011; 66(5): 759–777.
20. Disch C, Pfeil J, Kubach H, Koch T, Spicher U and Thiele O. Experimental investigations of a DISI engine in transient operation with regard to particle and gaseous engine-out emissions. *SAE Int J Engines* 2016; 9(1): 262–278.
21. Goschütz M, Schulz C and Kaiser SA. Endoscopic imaging of early flame propagation in a near-production engine. *SAE Int J Engines* 2014; 7: 351–365.
22. Schueck C, Koch T, Samenfink W, Schünemann E, Tafel S and Towae O. Optical investigations of soot formation mechanisms and possible countermeasures on a turbocharged port fuel injection SI engine. *SAE Int J Engines* 2016; 9: 2010–2021.
23. Dierksheide U, Meyer P, Hovestadt T and Hentschel W. Endoscopic 2D particle image velocimetry (PIV) flow

- field measurements in IC engines. *Exp Fluids* 2002; 33: 794–800.
24. Fach C, Rödel N, Schorr J, Krüger C, Dreizler A and Böhm B. Multi-parameter imaging of in-cylinder processes during transient engine operation for the investigation of soot formation. *Int J Engine Res* 2021; 146808742110199.
  25. Merola SS, Tornatore C, Marchitto L, Valentino G and Corcione FE. Experimental investigations of butanol-gasoline blends effects on the combustion process in a SI engine. *Int J Energy Environ Eng* 2012; 3: 6.
  26. Reeves M and Lawson NJ. On perspective errors in endoscopic PIV. *Comptes Rendus Mécanique* 2004; 332(9): 687–692.
  27. Adrian RJ. Particle-imaging techniques for experimental fluid mechanics. *Annu Rev Fluid Mech* 1991; 23(1): 261–304.
  28. Tsai R. A versatile camera calibration technique for high-accuracy 3D machine vision metrology using off-the-shelf TV cameras and lenses. *IEEE J Robot Automat* 1987; 3(4): 323–344.
  29. Willert CE. Assessment of camera models for use in planar velocimetry calibration. *Exp Fluids* 2006; 41: 135–143.
  30. Mounaïm-Rousselle C, Landry L, Halter F and Foucher F. Experimental characteristics of turbulent premixed flame in a boosted Spark-Ignition engine. *Proc Combust Inst* 2013; 34(2): 2941–2949.
  31. Schiffmann P, Reuss DL and Sick V. Empirical investigation of spark-ignited flame-initiation cycle-to-cycle variability in a homogeneous charge reciprocating engine. *Int J Engine Res* 2018; 19(5): 491–508.
  32. K Dabov, A Foi, V Katkovnik and K. Egiazarian Image restoration by sparse 3D transform-domain collaborative filtering. In: *Image processing: Algorithms and systems VI* (Vol. 6812, pp. 62–73). SPIE.
  33. Stiehl R, Bode J, Schorr J, Krüger C, Dreizler A and Böhm B. Influence of intake geometry variations on in-cylinder flow and flow–spray interactions in a stratified direct-injection spark-ignition engine captured by time-resolved particle image velocimetry. *Int J Engine Res* 2016; 17(9): 983–997.